



Strategies Towards Submicron Size and High-Performance Magnetic PGMA@Fe₃O₄@SiO₂-COOH Microspheres with Biological Application

Tianhao Xia¹ · Yunpeng Wang¹ · Pragati Awasthi¹ · Wenkun Dong² · Mengting Li² · Xvsheng Qiao¹ · Dong Chen² · Shisheng Ling² · Xianping Fan¹

Received: 17 October 2023 / Accepted: 18 December 2023 / Published online: 22 February 2024
© The Author(s), under exclusive licence to Springer Science+Business Media, LLC, part of Springer Nature 2024

Abstract

The separation of target substances is a significant biological detection procedure, where magnetic microspheres can act as high-performance separation materials. However, challenges are still kept to fulfill all the requirements. A submicron magnetic poly (glycidyl methacrylate) (PGMA) microsphere was synthesized in this investigation by utilizing three distinct techniques: in situ coprecipitation, electrostatic self-assembly, and silica surface coating. The PGMA microspheres were initially produced through a soap-free emulsion polymerization technique, wherein the coagulation process was governed by surface charge density. This factor additionally impacted the size and monodispersity of the microspheres. Then, we discovered that the capping agent sodium citrate (Na₃Cit) effectively regulated the superparamagnetism properties of magnetic microspheres; the critical size of the superparamagnetic was 10.9 nm. Furthermore, the concentration of Fe²⁺ and Fe³⁺ effectively regulated the saturation magnetization, a property that correlated with the nucleation rate of the Fe₃O₄ crystal. Additionally, we demonstrated that the pH regulated the electrostatic self-assembly, and it was suggested that positively charged PGMA-NH₂ microspheres and negatively charged Fe₃O₄ nanoparticles be tightly coupled. For application, the PGMA@Fe₃O₄ microspheres were subsequently coated with SiO₂, which had been surface-modified with carboxyl groups. The PGMA@Fe₃O₄ and carboxyl-modified microspheres exhibited saturated magnetization values of 23.73 and 17.73 emu/g, respectively. These microspheres have been effectively utilized for the extraction of DNA from various sources such as *Salmonella typhi*, monkeypox virus, and clinical swab samples, suggesting the potential of these microspheres for nucleic acid separation in the biomedical domain.

Keywords Superparamagnetic PGMA@Fe₃O₄ microspheres · pH-induced electrostatic self-assembly · In situ coprecipitation · Amino and carboxyl group · Nucleic acid separation

1 Introduction

In the biomedical field, DNA, RNA, proteins, enzymes, and polypeptides are usually regarded as crucial analytical parameters, consequently, the separation and purification of these substances constitute a significant method for biological detection, pathological research, and product development. Conventional separation techniques, such as lysis, chromatography, and various forms of liquid or solid-phase

extraction [1–4]. There are various drawbacks associated with this approach, including reduced efficiency, a complicated procedure, and a lack of autonomous functionality. Furthermore, certain chemicals employed in the extraction process exhibit potential risks to human health. To reduce the separation time and reliance on toxic reagents, nowadays magnetic isolation is applied more extensively, because of its notable attributes of high specificity, sensitivity, and efficiency. Meanwhile, the materials and instruments for this new technology are widely developed.

Biological magnetic isolation typically relies on superparamagnetic polymer microspheres that provide several desirable characteristics, including a high density of functional groups, rapid magnetic response, a large specific surface area, excellent disperse stability, and biocompatibility [5–7]. This type of material is mainly divided into

✉ Xvsheng Qiao
qiaoxus@zju.edu.cn

¹ State Key Laboratory of Silicon Materials & School of Materials Science and Engineering, Zhejiang University, Hangzhou 310058, China

² Assure Tech. (Hangzhou) Co., Ltd, Hangzhou 310015, China

core–shell (magnetic components serve as either the core or shell), sandwich, dispersion, and other structures. In recent years there has been a significant increase in scholarly interest globally regarding the utilization of various magnetic polymer microspheres for separation purposes. For instance, Ge et al. conducted a study in which they synthesized coordination compounds of M^{2+} ($M = \text{Ni, Co, Cu, and Zn}$) to modify polystyrene@ Fe_3O_4 microspheres. These changed microspheres exhibited a dispersion structure and were utilized for the isolation of histidine-tagged proteins. The researchers observed that the modified microspheres had notable characteristics such as high adsorption capacity, selectivity, and stability [8]. Zandieh et al. used a solvothermal method to prepare submicron Fe_3O_4 nanoparticles, then in situ coated polydopamine on the surface of particles, finally modified with spherical nucleic acids to extract target DNA, these core–shell microspheres exhibited notable extraction efficacy and selectivity [9]. However, there are still several shortcomings in the microspheres studied and used now. For core–shell microspheres, it is hard to synthesize Fe_3O_4 particles with a size larger than 200 nm, thus the bulk size or magnetic contents cannot be controlled in a wide range [10–12]. To disperse microspheres, it is necessary to combine Fe_3O_4 nanoparticles with monomers prior to the polymerization procedure. This requires the modification of Fe_3O_4 nanoparticles with oleophilic chemicals, hence imposing limitations on the magnetic components. [13–15]. To solve the shortcomings, in the 1980s Ugelstad et al. developed a new type of core–shell microspheres consisting of polymer microspheres as cores and Fe_3O_4 nanoparticles as shells, which indicates that the size and monodispersity only depend on polymer microspheres [16, 17]. Besides, the magnetic contents can be easily controlled up to more than 30% [18]. To avoid the magnetic contents being oxidized as well as contact with the detection environment directly, inorganic materials like SiO_2 and TiO_2 are usually used as protective layers on the surface of polymer@ Fe_3O_4 microspheres to form sandwich structures [19, 20].

The Fe_3O_4 shell in the composite microspheres is mainly synthesized by an in situ coprecipitation method, which has the same mechanism as the traditional coprecipitation method, i.e., firstly polymer microspheres were mixed with Fe^{2+} and Fe^{3+} solutions and then a fast coprecipitation reacted under a special environment with high temperature and pH range of 8–14 [21]. This method was widely used and has developed into products like Dynabeads® [22]. However, up to now, most of the studies of in situ coprecipitation magnetic polymer microspheres were based on micron-sized polymer spheres [23–26], and there are few studies focused on submicron and monodispersed polymer spheres, also the bonding mechanism of Fe_3O_4 nanoparticles and polymer microspheres has not been well explained. Therefore, it is imperative to conduct thorough investigations

on materials with elevated Fe_3O_4 concentrations and submicron-sized magnetic polymer microspheres. In this study, our target is to synthesize monodispersed and superparamagnetic Fe_3O_4 @polymer microspheres with a controllable size range of 300–600 nm, also increasing the Fe_3O_4 contents in the microspheres. The soap-free emulsion method was used to prepare PGMA microspheres as the template, and then the microspheres were modified by ethylenediamine (EDA) to fix amino groups, finally, the PGMA- NH_2 microspheres were added to Fe^{2+} and Fe^{3+} solutions, and Fe_3O_4 contents were generated by an in situ coprecipitation method. We firstly reveal the combination mechanism of Fe_3O_4 nanoparticles and PGMA microspheres and functionalize these magnetic microspheres by carboxyl groups to separate DNA in *Salmonella typhi*, monkeypox virus, and clinical swab samples.

2 Experimental

2.1 Materials and Reagents

Ferrous chloride tetrahydrate ($\text{FeCl}_2 \cdot 4\text{H}_2\text{O}$, 98%), ferric chloride hexahydrate ($\text{FeCl}_3 \cdot 6\text{H}_2\text{O}$, 99%) and glycidyl methacrylate (GMA, 97%) were purchased from Shanghai Macklin Biochemical Reagent Co. Ltd. Potassium peroxydisulfate (KPS, AR), ethylenediamine (EDA, AR) and ethyl alcohol (EtOH, AR) were purchased from Sinopharm Chemical Reagent Co. Ltd. Sodium citrate (Na_3Cit , 98%), ammonia ($\text{NH}_3 \cdot \text{H}_2\text{O}$, 25–28 wt%), tetraethyl orthosilicate (TEOS, 99%), 3-aminopropyl triethoxysilane (APTES, 99%), succinic anhydride (SA, 99%), N, N-dimethylformamide (DMF, 99.9%) were purchased from Shanghai Aladdin Biochemical Reagent Co. Ltd. HCl titration solution (0.01036 M), NaOH titration solution (0.009435 M), and deionized water was made by laboratory.

2.2 Preparation of Monodispersed PGMA and PGMA- NH_2 Microspheres

PGMA microspheres with different sizes were produced by soap-free emulsion polymerization [27, 28]. In our method, a certain volume of GMA and 45 mL of H_2O were first mixed in a four-neck flask, and argon was purged for 30 min to create an O_2 -free environment. Then the mixture was heated to 70 °C, and 5 mL KPS solution (2.0 wt%) was added to the flask as an initiator. Keep the polymerization under mechanical stirring (500 rpm) and reflux condensation for 4.5 h, and the products were centrifuged and washed several times with deionized water, finally dispersed in 50 mL of deionized water. About 1.2 g of PGMA microspheres were dispersed in 36 mL of H_2O in a four-neck flask and then added 36 mL of EDA to the flask. Heated the solution

to 90 °C and maintained stirring for 12 h to form the resulting products. The PGMA–NH₂ microspheres were centrifuged and washed several times with deionized water and dispersed in deionized water.

2.3 In Situ Coprecipitation to Synthesize PGMA@Fe₃O₄ Microspheres

An amount of 1.0 g PGMA–NH₂ microspheres was mixed with 20 mL of H₂O in a four-neck flask, then added 50 mL of Fe³⁺ and Fe²⁺ solution ($c(\text{Fe}^{3+}): c(\text{Fe}^{2+}) = 1.6: 1$) to the dispersion liquid, and cooled down to 5–10 °C in an ice bath. The flask was evacuated for 20 min, heated to 75 °C, and purged argon simultaneously. Added Na₃Cit to the mixture and then added NH₃·H₂O to precipitate the Fe³⁺ and Fe²⁺ ions. The reaction was retained for 1.5 h, and the composite microsphere products were washed several times by magnetic isolation to remove ammonia. Finally, the PGMA@Fe₃O₄ microspheres were dispersed in about 50 mL of deionized water.

2.4 Synthesis of PGMA@Fe₃O₄@SiO₂–COOH Microspheres by Stöber Method and Amidation Reaction

PGMA@Fe₃O₄@SiO₂–NH₂ microspheres were synthesized by means of a modified Stöber method [29, 30]. Briefly, 0.10 g of PGMA@Fe₃O₄ microspheres were added to a mixed solution including 35 mL of EtOH, 4 mL of deionized water, and 2 mL of ammonia in a four-neck flask. 0.1 mL of TEOS was dissolved in 5 mL of EtOH and added to the mixture in the flask dropwise. The hydrolysis reaction was maintained at 30 °C for 18 h, then 0.05 mL of APTES was dissolved in 2.5 mL of EtOH and added to the mixture like TEOS. After 6 h, the PGMA@Fe₃O₄@SiO₂–NH₂ microspheres were prepared, washed several times, and dispersed in deionized water.

Weighed 1.5 g of SA to dissolve in 30 mL DMF, the solution was stirred for 4 h and transferred to a four-neck flask, and then 20 mL of DMF was supplied. Took 0.1 g of PGMA@Fe₃O₄@SiO₂–NH₂ microspheres and washed by DMF three times, dispersed in 10 mL of DMF, and added to the SA solution dropwise. Kept the reaction at room temperature, and argon charged several times. The final products were washed and dispersed in deionized water at a low temperature (2–4 °C).

2.5 Characterization Methods

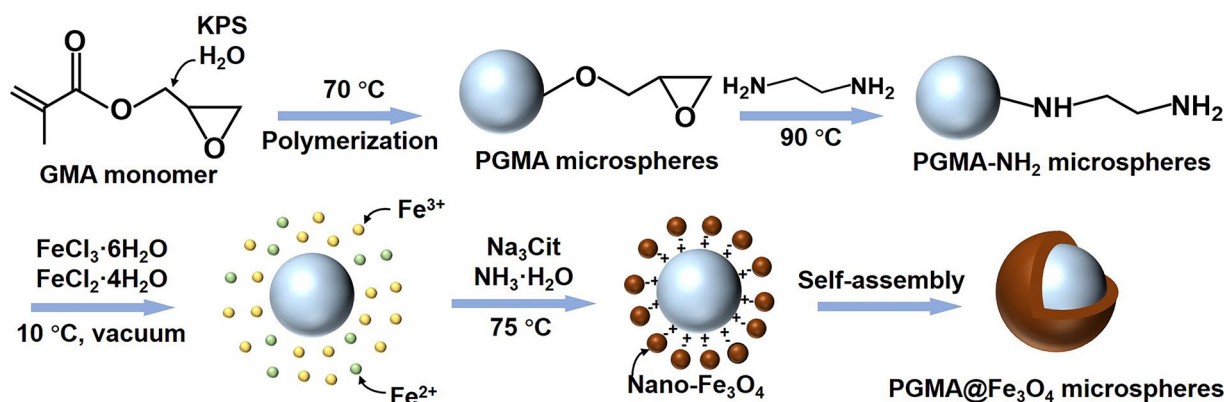
The morphology of polymer and composite samples was characterized by Zeiss GeminiSEM 360 scanning electron microscope (SEM) and the structure of magnetic microspheres was determined by JEOL JEM-2010 transmission

electron microscope (TEM). The distribution, chemical state, and contents of different elements in samples were analysed by energy dispersive X-ray spectrometer (EDS), X-ray photoelectron spectrometer (XPS, Thermo Fisher Escalab 250Xi), and X-ray Fluorescence Spectrometer (XRF, Bruker S8 TIGER), respectively. The crystal structure of Fe₃O₄ contents was obtained with a Shimadzu XRD-6000 diffractometer equipped with Cu K_α radiation. The FT-IR spectra of PGMA and magnetic microspheres were detected by Nicolet iS5 FT-IR spectrophotometer between 4000 and 400 cm⁻¹. The magnetic contents and weight loss in high temperature of PGMA@Fe₃O₄ microspheres were measured by Netzsch STA-2500 thermal analyser from room temperature to 800 °C at a heating rate of 5 °C/min under nitrogen. The magnetic hysteresis loops of the samples are measured with a vibrating sample magnetometer (VSM, Lakeshore, Model 7300) with a field up to 2.0 T.

The dispersion stability in water solutions of magnetic microspheres was measured by standing the dispersion liquid for 30 min, 3 h, and 6 h at room temperature, and the magnetic responsiveness was detected by magnet attraction for 30 s, 1.5 min, and 3 min. Acid–base titration was used to measure the contents of primary amine groups in PGMA@Fe₃O₄@SiO₂–NH₂ microspheres, and the concentration of carboxyl groups in PGMA@Fe₃O₄@SiO₂–COOH microspheres was calculated by the results of potentiometric titration.

2.6 DNA Extraction Experiment

The biological samples were combined with a lysis solution in order to facilitate the separation of cells or viruses. Subsequently, a substantial amount of polyethylene glycol (PEG) and NaCl were introduced to induce a high concentration of salt and viscosity within the mixture. In this investigation, the solution was augmented by magnetic microspheres, namely PGMA@Fe₃O₄@SiO₂–COOH microspheres synthesized within the scope of this research, or magnetic microsphere products that are commercially accessible. Following that, the microspheres were subjected to the adsorption of DNA molecules onto their surface. A magnetic field was employed to facilitate the separation process, followed by the extraction of the liquid supernatant. Subsequently, distilled water was used to separate the DNA from the microspheres. The DNA concentration of the sample was detected by an Allsheng Nano-300 microspectrophotometer. Subsequently, polymerase chain reaction (PCR) amplification was performed on the sample to attain a targeted concentration. The precise number of amplification cycles was ascertained. Images were captured during gel electrophoresis experiments utilizing 1.0 wt% agarose gels to assess the DNA extraction purity of various microspheres subsequent to PCR amplification.



Scheme 1 The procedure of preparing core-shell PGMA@Fe₃O₄ microspheres

3 Results and Discussion

3.1 Characterization of PGMA and PGMA@Fe₃O₄ Microspheres

As Scheme. 1 illustrated, the core-shell PGMA@Fe₃O₄ microspheres can be synthesized through an electrostatic self-assembly method. Firstly, the blank PGMA microspheres were prepared through soap-free polymerization and modified by EDA. Then, the PGMA@Fe₃O₄ microspheres with core-shell structure mainly self-assembled with positively charged PGMA and negatively charged Fe₃O₄, where EDA and Na₃Cit act as surfactant modifiers, respectively. Herein, PGMA microspheres are taken as the template to support magnetic Fe₃O₄ nanoparticles as shell layers on the spherical surface.

During the soap-free polymerization, the acquisition of a well-defined size distribution of PGMA microspheres is achievable through the surface charge density determined coagulation process. When the GMA volume is 2.25 mL, 4.5 mL, and 6.75 mL (Fig. 1a–c), the PGMA microspheres, are monodispersed and the average size is about 250 nm, 400 nm, and 600 nm, respectively. However, Fig. 1d shows that increasing the GMA volume to 9 mL will result in polydispersity of PGMA microspheres. Such this variation of size and monodispersity of soap-free polymerized PGMA microspheres can be explained by the particle coagulation theory [31–33], that is, primary nuclei were formed by precipitation of large chain length polymers, while the ionic initiator provided surface charge to keep dispersity. Under a high GMA concentration, to maintain the thickness of the electrical double layer, the particles coagulated to a larger size to decrease specific surface area and promoted monodispersity by self-sharpening effects. While the GMA concentration was too high, the charge density of primary particles was too low to maintain stability, and the particles coagulate excessively, leading to the polydispersity of final

microspheres. Therefore, the inner mechanism of controlling the size and monodispersity is the adjusting of surface charge density. Meanwhile, maintaining the GMA concentration to synthesize monodispersed PGMA microspheres under a fixed initiator amount is significant.

To fabricate electrostatically self-assembled PGMA@Fe₃O₄ microspheres, we prepared positively charged PGMA–NH₂ microspheres, through an EDA triggered a ring-open reaction of epoxy groups on the surface of PGMA microspheres. From the SEM (Fig. 1e–h) observation, the size and morphology of PGMA–NH₂ microspheres almost appear no changes. For the next step, the PGMA@Fe₃O₄ microspheres were electrostatically self-assembled through an in situ coprecipitation of Cit³⁻ capped and negatively charged Fe₃O₄ nanoparticles on the surface of PGMA–NH₂ microspheres. From the SEM (Fig. 1i–l) and TEM images (Fig. 1m–p), the Fe₃O₄ nanoparticles are mainly distributed on the surface of PGMA microspheres. It makes the whole composite microspheres with rough surfaces and confirms the formation of core-shell structures. There are also some deeply-colored particles in the inner layer, indicating a small part of Fe₃O₄ nanoparticles are impregnated into PGMA–NH₂ microspheres.

3.2 Crystalline and Magnetic Properties of PGMA@Fe₃O₄ Microspheres

Superparamagnetism properties are well guaranteed when the grain sizes of Fe₃O₄ nanocrystals are well controlled below the critical size, i.e., 10.9 nm. Here we carried out the Na₃Cit suppressed crystal growth strategy to control Fe₃O₄ nanocrystals with sizes below 10.9 nm. In Fig. 2a, the diffraction peaks match well with standard PDF cards of Fe₃O₄ crystal, and intensity decreases as the Na₃Cit amount increases. The grain size was calculated by the Debye–Scherrer formula. It also decreases with a higher Na₃Cit amount (see Fig. 2b). The essence is concluded by

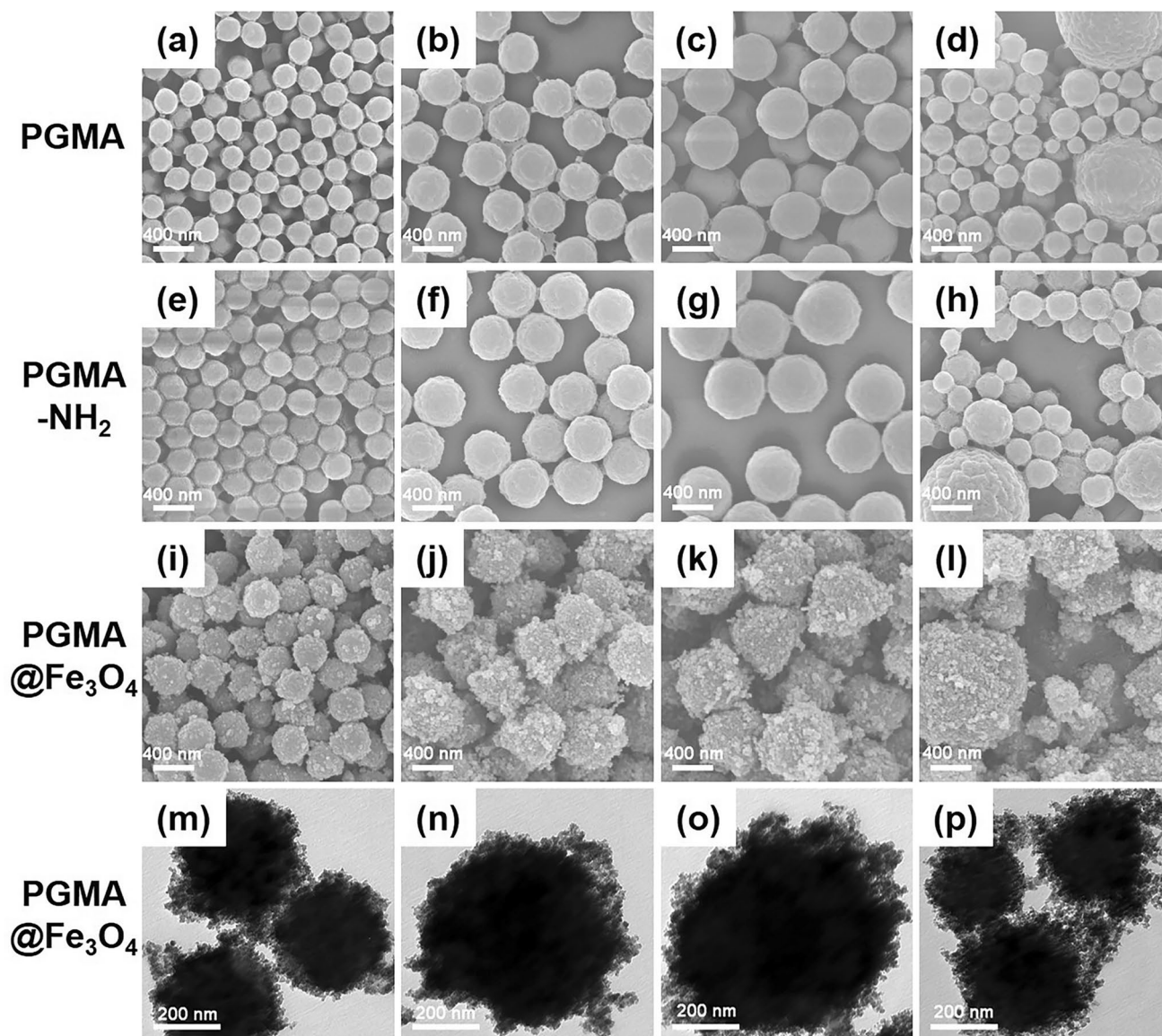


Fig. 1 The SEM and TEM images of PGMA, PGMA-NH₂, and PGMA@Fe₃O₄ microspheres for GMA volume of **a, e, i, m** 2.25 mL; **b, f, j, n** 4.5 mL; **c, g, k, o** 6.75 mL; **d, h, l, p** 9 mL

Cornell et al. [34]: Cit³⁻ acts as the capping agent and one Cit³⁻ ion has a strong coordination effect with one or two Fe ions (Fe²⁺ or Fe³⁺) in the mixture, once ammonia is added to nucleate, the coordinated complex will be distributed on the surface of Fe₃O₄ nuclei, and Cit³⁻ produces extra COO⁻ to promote electrostatic repulsion, therefore the growth of Fe₃O₄ crystal is inhibited [35–37].

The addition of Na₃Cit ≥ 0.050 g is evidenced to get the Fe₃O₄ grain size below the critical value, thus the coercive force (H_c) and remanent magnetization (M_r) would be meager to exhibit the superparamagnetic behaviors. As the magnetic domain theory described, bulk Fe₃O₄ has a multi-domain structure. While the grain size Fe₃O₄ decreases, Fe₃O₄ is transferred to a monodomain structure and the

surface spin disorder will be increased [38]. Finally, the grain size reaches a critical value, and Fe₃O₄ materials will have an unstable magnetic state without an external magnetic field, i.e., superparamagnetism. In Fig. 2c, it is obvious that the superparamagnetic critical size is at about 10.9 nm, as described in the previous experimental results [39, 40]. Nevertheless, when the grain size of Fe₃O₄ is smaller than this value, M_r and H_c are near zero; when the grain size is more significant, the M_r and H_c increase linearly. From the curves in Fig. 2d, the saturation magnetization (M_s) is also relative to the Na₃Cit amount, which is due to the finite size effect and crystal defects [41]. In summary, to keep the superparamagnetism and high M_s of PGMA@Fe₃O₄ microspheres, the appropriate Na₃Cit amount should be 0.050 g.

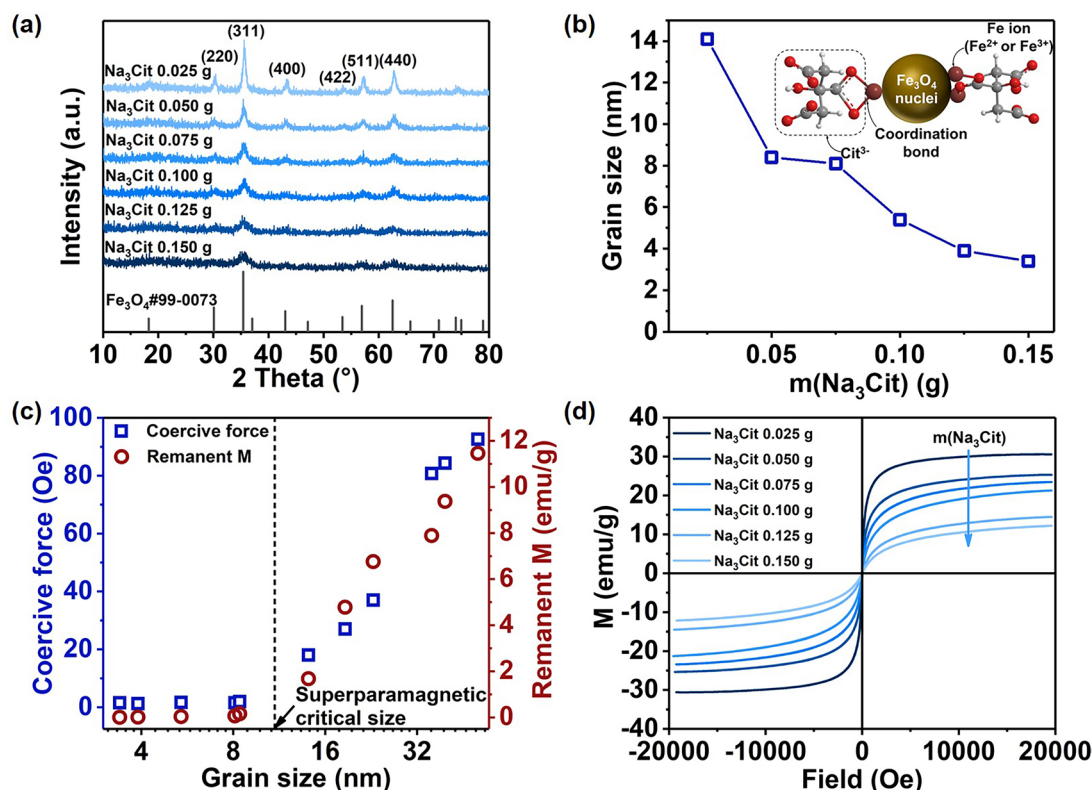


Fig. 2 The XRD patterns (a), variation of Fe₃O₄ grain size (b), remanent magnetization and coercive force (c), hysteresis loop (d) of PGMA@Fe₃O₄ microspheres with different Na₃Cit amount

Besides the superparamagnetism, saturation magnetization is also essential for PGMA@Fe₃O₄ microspheres, which can be well strengthened by increasing the Fe concentration (c(Fe)). It is correlated with the nucleation rate of Fe₃O₄ crystal. Figure 3a shows that when the ammonia volume added to the mixture is fixed, the nucleation process of low and high c(Fe) mixture are different, this result can be interpreted by the classical nucleation-growth theory: A higher concentration will provide a higher degree of supersaturation, thus the absolute value of Gibbs free energy (ΔG) is raised and more Fe₃O₄ nuclei will form in the initial period [42], after growth, there will be more amount of grains in the distribution system. From Fig. 3b–d, it can be concluded that the M_s and Fe₃O₄ contents are strongly relative to the c(Fe), which is the result of the nucleation process controlled by supersaturation.

3.3 The Synthesis Mechanism of PGMA@Fe₃O₄ Microspheres

A pH-guided electrostatic self-assembly strategy is proposed to tightly couple the PGMA–NH₂ microspheres with positive charges and Fe₃O₄ microspheres with negative charges. From the curves in Fig. 4a, the isoelectric point of PGMA–NH₂ microspheres and Fe₃O₄@Na₃Cit nanoparticles

are pH 9.51 and pH 6.24, respectively. This result indicates that within the pH range of 6.24 to 9.5, both the microspheres and nanoparticles carry opposite surface charges, and the self-assembly process will present. The reason for this phenomenon is that the –NH₂ groups can capture protons from the solution through lone pairs in nitrogen atoms. Thus, the amino groups are protonated, and microspheres carry an extra positive charge in the alkaline environment [43]. Meanwhile, Na₃Cit acts as the ionic surfactant combined with Fe₃O₄ nanoparticles and supplies extra negative charge by uncoordinated carboxyl groups in Cit³⁻, therefore the isoelectric point is in an acidic atmosphere. It can be clearly seen from Fig. 4b that the attraction between –COO⁻ mainly generates the electrostatic self-assembly of a group of Fe₃O₄ nanoparticles and –NH₃⁺ group of PGMA microspheres [44]. Also, the isoelectric point of PGMA@Fe₃O₄ microspheres is pH 8.01, which proves the self-assembly is completed. To make the coprecipitation reaction adequate, and create a strong driving force for self-assembly, we concluded the appropriate synthesis pH range was 8–9.

To work out the optimum pH range of the electrostatic self-assembly, the introduced ammonia volume and Fe concentration for coprecipitation were stepwise investigated within the pH value of 3–10. In Fig. 4c, the reaction system's final pH increased as more ammonia was added. When V(NH₃·H₂O)

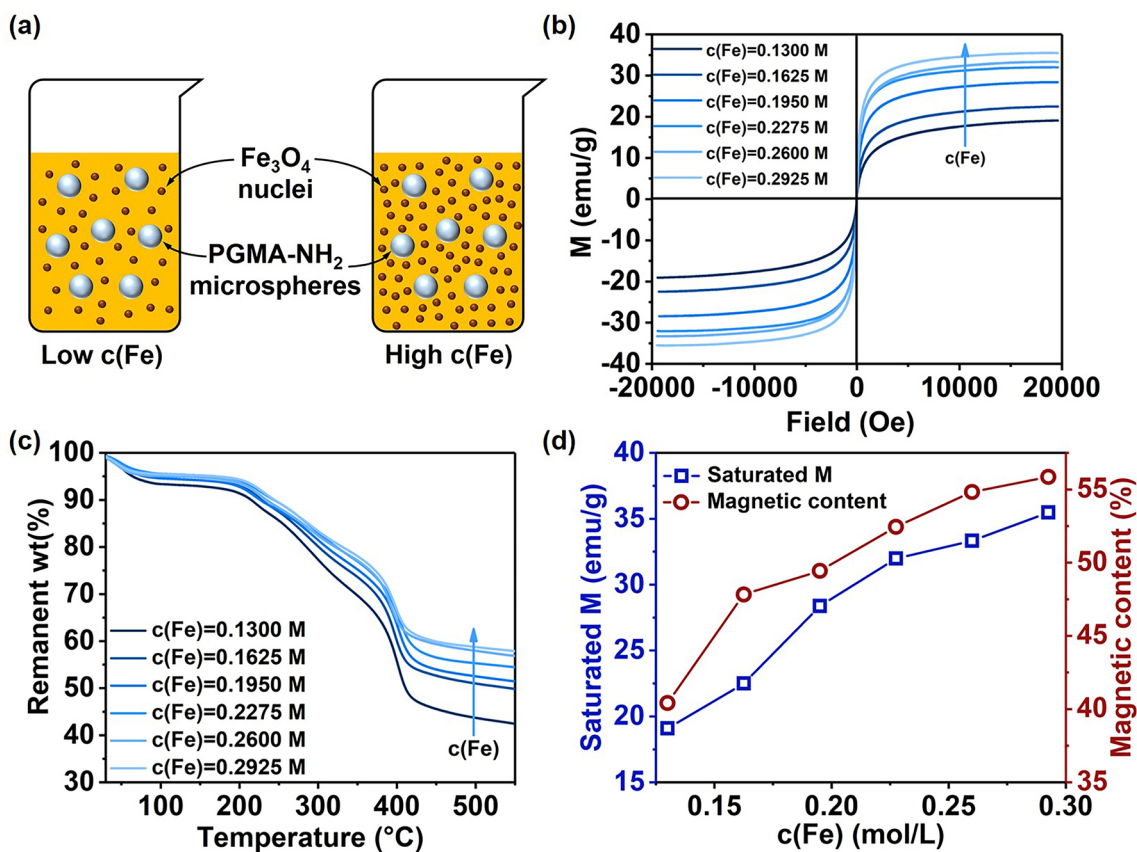


Fig. 3 The scheme of nucleation (a), hysteresis loop (b), thermogravimetric curve (c), variation of saturated magnetization and magnetic content (d) of PGMA@Fe₃O₄ microspheres with different c(Fe)

is 1 mL, the final pH is only 6.30, where the alkalinity is not high enough to form Fe₃O₄, so the conversion rate is low. Increasing V(NH₃·H₂O) to 2 mL, the final pH is 8.51, proving that the coprecipitation reaction is adequate (the suitable pH for coprecipitation is 8–14), also the Zeta potential of PGMA–NH₂ and Fe₃O₄@Na₃Cit are precisely opposite, thus self-assembly occurred once the Fe₃O₄ nanoparticles formed. Continue to increase V(NH₃·H₂O) to 4–6 mL, and the final pH will be higher than 9.0, where the zeta potential of PGMA–NH₂ microspheres decreases sharply. Therefore, the electrostatic self-assembly will be restrained. In Fig. 4d, when the V(NH₃·H₂O) is fixed, the final pH will decrease as c(Fe) increases, on account of the hydrolysis of Fe³⁺ and Fe²⁺ producing extra H⁺. However, the c(Fe) is not the higher, the better, because the initial coating of Fe₃O₄ nanoparticles will gradually neutralize the positive charge and decrease the Zeta potential of composite microspheres, hence the self-assembly is not continuous.

3.4 Characterization and Properties of PGMA@Fe₃O₄@SiO₂–COOH Microspheres

In the above sections, we practically optimized and discussed the synthesis of PGMA@Fe₃O₄ microspheres through the critical size and pH-guided electrostatic assembly strategies. However, the PGMA@Fe₃O₄ microspheres tended to clump and precipitate, resulting in a loss of uniform dispersion. This characteristic renders them unsuitable for meeting the requirements of biological magnetic separation. Whereupon, further modification is necessary for the submicron PGMA@Fe₃O₄ microspheres to get a long-term uniform dispersion. We thus practiced a silica-coating strategy to get a type of carboxyl functionalized microspheres.

The variation of elements and chemical bonds on the surface during the synthesis process of carboxyl-modified microspheres could be verified by EDS and XPS analysis, and the results indicate that SiO₂ has successfully coated

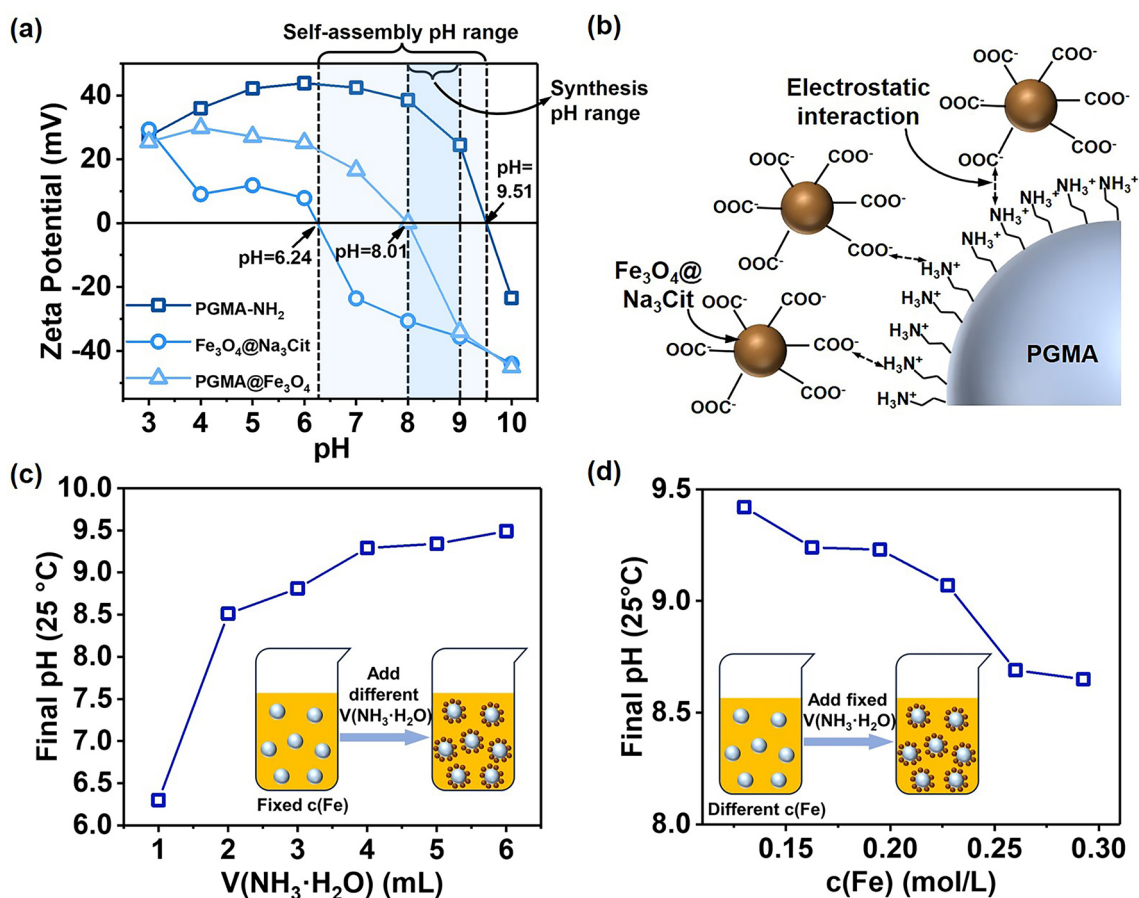


Fig. 4 Zeta potential of PGMA-NH₂ microspheres, Fe₃O₄@Na₃Cit nanoparticles and PGMA@Fe₃O₄ microspheres in different pH (a); the scheme of self-assembly process (b); the final pH at different V(NH₃·H₂O) (c) and c(Fe) (d)

onto the surface of PGMA@Fe₃O₄ microspheres, the amine and carboxyl functionalization reactions also mainly occur at the surface of the microspheres. In EDS images (Fig. 5a) and elements percentage tables (Table S2), Fe signals prove the Fe₃O₄ contents in the microspheres, Si signals are obviously strengthened after coated with SiO₂ and functionalized by APTES, and intensity of Fe, N, O, Si signals have almost no change after carboxyl modification, which could certify that amidation reaction only transfers primary amine groups (-NH₂) into secondary amine groups (-NH-). However, the amine groups will not fall off the surface of microspheres. XPS spectra (Fig. 5b) show that there are two peaks at 723.96 eV and 710.28 eV, which are ascribed to the Fe 2p_{1/2} and Fe 2p_{3/2} of Fe₃O₄ constituents on the surface of microspheres, and indicates the existence of both Fe²⁺ and Fe³⁺ ions [45]. However, for PGMA@Fe₃O₄@SiO₂-NH₂ and PGMA@Fe₃O₄@SiO₂-COOH microspheres, the Fe peaks are severely weakened due to the shielding by SiO₂ on the surface. The slight displacement of N 1s peaks from 399.27 eV (PGMA@Fe₃O₄@SiO₂-NH₂) to 399.96 eV (PGMA@Fe₃O₄@SiO₂-COOH) could be

attributed to the conversion from primary amine to secondary amine groups. For O 1s peaks, the substantial displacement from 529.58 eV (PGMA@Fe₃O₄) to 531.93 eV (PGMA@Fe₃O₄@SiO₂-NH₂) is mainly related to the decrease of lattice oxygen in Fe₃O₄ [46] and increase of Si-O bonds [47] on the surface, after amidation reaction the O 1s peak moves to 532.39 eV because of the influence of carboxyl groups. The Si 2p peaks only exist in the spectra of the microspheres after silica coating, further proving the distribution of SiO₂ in PGMA@Fe₃O₄@SiO₂-NH₂ and PGMA@Fe₃O₄@SiO₂-COOH microspheres. XRF analysis was performed to determine the concentrations of Fe and Si in various microspheres precisely; the results (Table 1) indicate that the application of a SiO₂ coating will undoubtedly reduce the magnetic concentrations.

Following the application of a SiO₂-coated and -COOH-modified surface, the magnetic microspheres exhibited a marked enhancement in their smoothness and the appearance of novel functional groups designed to impede aggregation. SEM images in Fig. 6a and b reveal that after SiO₂ coating, the average size of magnetic microspheres increases

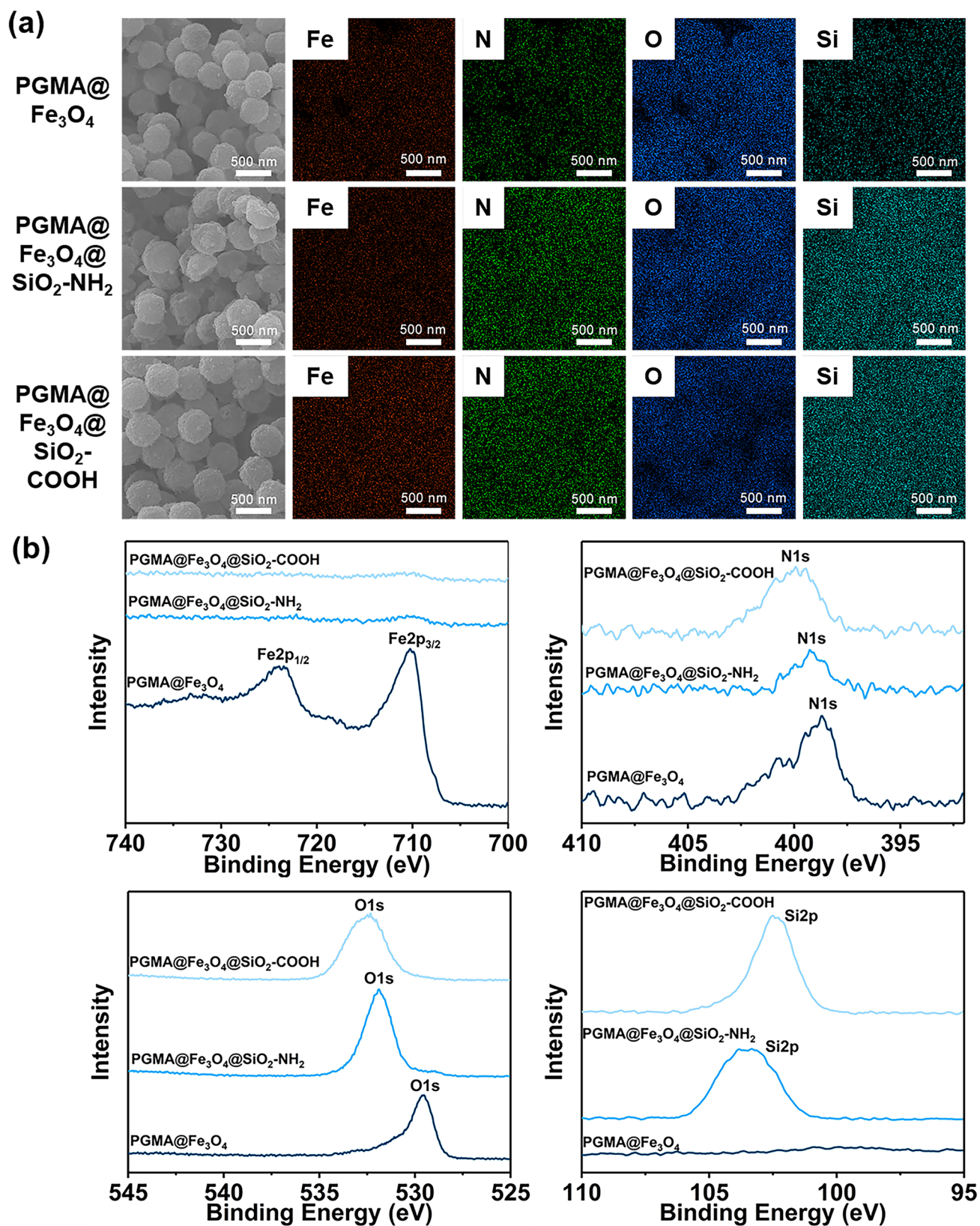


Fig. 5 **a** EDS surface scanning maps of PGMA@Fe₃O₄, PGMA@Fe₃O₄@SiO₂-NH₂, PGMA@Fe₃O₄@SiO₂-COOH microspheres; **b** XPS spectra of PGMA@Fe₃O₄, PGMA@Fe₃O₄@SiO₂-NH₂, PGMA@Fe₃O₄@SiO₂-COOH microspheres

Table 1 XRF data of Fe and Si contents in different microspheres

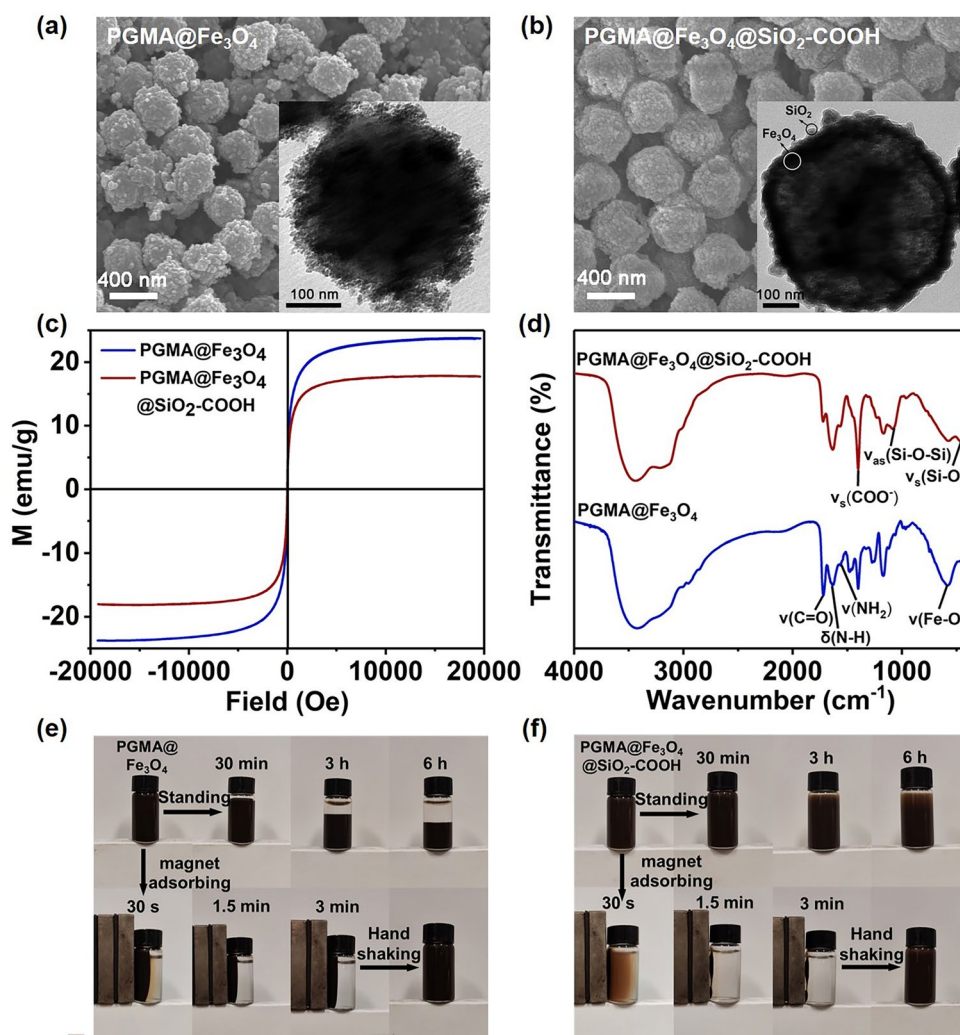
Microspheres	Fe ₂ O ₃ wt%	SiO ₂ wt%	Fe wt%	Si wt%
PGMA@Fe ₃ O ₄	36.1	0.124	25.249	0.058
PGMA@Fe ₃ O ₄ @SiO ₂ -NH ₂	9.08	9.69	6.351	4.529
PGMA@Fe ₃ O ₄ @SiO ₂ -COOH	8.89	5.36	6.218	2.505

from 380 to 420 nm, and the surface is much smoother. TEM image of PGMA@Fe₃O₄@SiO₂-COOH microspheres (Fig. 6b) obviously shows the light-colored SiO₂ layer on the surface of the microspheres, the average thickness is about 10 nm. The superparamagnetic nature of PGMA@Fe₃O₄ and PGMA@Fe₃O₄@SiO₂-COOH microspheres is evident from Fig. 6c; their respective saturation magnetizations are 23.73 and 17.73 emu/g. The M_s of carboxyl microspheres is lower because the SiO₂ coating makes less magnetic content. Figure 6d indicates that after SiO₂ coating and carboxyl

functionalized, the Si–O and Si–O–Si vibration peaks can be observed in turn at 465 and 1078 cm⁻¹ [48], and the carboxyl characteristic peak at 1399 cm⁻¹ is strengthened while stretching vibration peak of C=O bond at 1730 cm⁻¹ is weakened. In contrast, epoxy groups exhibit distinct vibration peaks at 845 and 910 cm⁻¹ [25] (Fig. S1), for original PGMA microspheres; these two peaks vanish after EDA reaction, demonstrating that the ring-open reaction between epoxy and amino groups is complete.

After being functionalized, the microspheres obtain much higher stability in aqueous solutions, because of the raised concentration of functional groups and surface charge density. Figure 6e and f show that the PGMA@Fe₃O₄@SiO₂-COOH microspheres have higher stability than PGMA@Fe₃O₄ microspheres and can be well dispersed for at least 30 min. The underlying mechanism might be attributed to the alteration caused by the amidation reaction which results in an increase in the carboxyl density of microspheres and restores negative charges to the surface for stable dispersion. The carboxyl microspheres have a

Fig. 6 The SEM and TEM image (a, b), hysteresis loops (c), and FTIR spectrum (d) of PGMA@Fe₃O₄ and PGMA@Fe₃O₄@SiO₂-COOH microspheres; photographs of PGMA@Fe₃O₄ and PGMA@Fe₃O₄@SiO₂-COOH microspheres after standing, magnet attraction and shaking (e, f)



relatively high magnetic response within 1.5 min, almost the same as $\text{PGMA}@Fe_3O_4$ microspheres. To precisely measure the concentration of amine and carboxyl groups in the microspheres, the $\text{PGMA}@Fe_3O_4@SiO_2-NH_2$ and $\text{PGMA}@Fe_3O_4@SiO_2-COOH$ microspheres were respectively reacted with HCl and NaOH for 24 h, then a titration was carried out with acid–base neutralization reaction. The potentiometric titration curve (Fig. S3) reveals a platform zone characterized by minimal conductance variation, where the $-COOH$ groups on the microspheres react with HCl. The volume of HCl in this region is 800 μL , and the prime amine concentration of $\text{PGMA}@Fe_3O_4@SiO_2-NH_2$ microspheres is 1.458 mmol/g. Consequently, the carboxyl concentration of $\text{PGMA}@Fe_3O_4@SiO_2-COOH$ microspheres is calculated to be 0.829 mmol/g. This value signifies that more than half of the prime amine groups have reacted with SA and converted into carboxyl groups.

3.5 Bioapplication of $\text{PGMA}@Fe_3O_4@SiO_2-COOH$ Microspheres

DNA separation was performed using the $\text{PGMA}@Fe_3O_4@SiO_2-COOH$ microspheres that were synthesized in this investigation due to their superior magnetic properties and

high dispersion stability. The isolation process was mainly based on the cation bridge interaction between the carboxyl group in microspheres and the phosphate group in DNA under a high salt concentration environment [49]. As Fig. 7a illustrates, the study established the DNA absorption environment through the utilization of high-concentration NaCl solutions, while PEG was included to enhance viscosity. Carboxyl microspheres and DNA samples possess negative charges, which result in their attraction to each other and the formation of cation bridges through the binding of Na^+ ions. Once the salt solution is removed, the structure becomes unstable, allowing the absorbed DNA to be released by pure water.

We compared the prepared microspheres with the commercial products (BeaverBeads™ Mag COOH), where the DNA samples from *Salmonella typhi*, monkeypox virus, and epithelial cells in clinical swabs were detected. As a result, our microspheres show comparable or better performance. In order to assess the efficacy of the extraction process, we devised a program that utilized a predetermined combination and elution time to extract DNA from various samples. Subsequently, the concentration of DNA in the final eluent was determined via spectrophotometric means, with cycle threshold (C_T) serving as the standard index. C_T

Fig. 7 **a** Scheme of the whole process of DNA isolation in cell samples; **b** agarose gel electrophoresis of different DNA samples isolated by magnetic microspheres. Lane M: DNA molecular weight marker; lane 1: DNA isolated from *Salmonella typhi* by carboxyl microspheres in this work; lane 2: DNA isolated from *Salmonella typhi* by Mag COOH; lane 3: DNA isolated from monkeypox virus by carboxyl microspheres in this work; lane 4: DNA isolated from monkeypox virus by Mag COOH; lane 5: DNA isolated from epithelial cell by carboxyl microspheres in this work; lane 6: DNA isolated from epithelial cell by Mag COOH

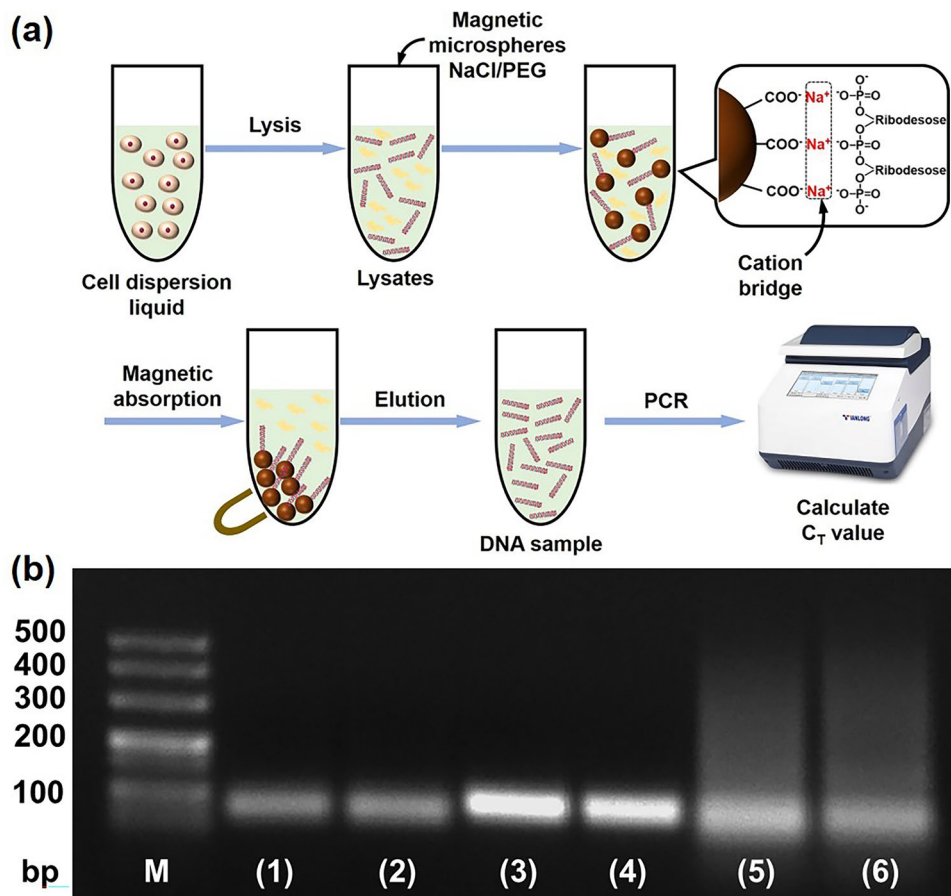


Table 2 The extraction concentration and average C_T of Mag COOH and PGMA@Fe₃O₄@SiO₂-COOH microspheres in isolation of Salmonella typhi DNA, monkeypox virus, and epithelial cell

Isolation samples	Mag COOH	This work
Salmonella typhi		
Average C_T	21.92	21.82
DNA extraction contents (ng/ μ L)	0.995	1.066
Monkeypox virus		
Average C_T	21.01	21.21
DNA extraction contents (ng/ μ L)	1.537	0.555
Epithelial cell		
Average C_T	31.31	29.59
DNA extraction contents (ng/ μ L)	1.794	1.948

corresponded to the number of cyclic amplifications required to attain the detecting concentration [50]. As is shown in Table 2, when the microspheres synthesized in our work were used to detect Salmonella typhi and epithelial cell samples, the average C_T was lower than the detection using Mag COOH, also the DNA extraction concentration was higher, and in the monkeypox virus sample the average C_T was only slightly higher with a lower DNA extraction concentration. The agarose gel electrophoresis characterized the purity of extracted DNA, as shown in Fig. 7b. Narrow DNA bands are observed at about 50–100 bp for Salmonella typhi and monkeypox virus samples, representing the high isolation purity. However, the DNA bands of epithelial cell samples isolated from two kinds of microspheres are both broad with a lower purity. The microspheres synthesized in our study have the potential to be utilized in the isolation of nucleic acid from bacteria, viruses, and cells, as demonstrated by these results. In light of recent reports of a similar nature, we intend to integrate our research with rare earth fluorescent nanoparticles in the future to develop a sensor system [51], furthermore, we intend to broaden the scope of detection to include RNA, with a specific focus on RNA detection in the context of influenza [52] and COVID-19 virus [52, 53]. In the interim, we will validate the detection selectivity of the carboxyl microspheres that we have synthesized in interference conditions prior to any further modifications.

4 Conclusions

In brief, we described a category of submicron monodispersed PGMA@Fe₃O₄ core-shell microspheres that were produced via silica-coated surface modification, in situ coprecipitation, and electrostatic self-assembly. Through the adsorption of Cit³⁻ ligands onto the crystalline surface, the growth of Fe₃O₄ nanocrystals can be well suppressed and their grains can be well controlled below 10.9 nm, the

so-called superparamagnetic critical size. This facilitates the attainment of remanent magnetization and coercive force values that approach zero. The PGMA@Fe₃O₄ core-shell microspheres are electrostatically assembled with the negatively charged Fe₃O₄ onto the surface of positively charged PGMA-NH₂ microspheres. The self-assembly process effectively occurs in the pH range of 6.24–9.51. By progressively increasing the Fe₃O₄ content and applying a surface coating of SiO₂ and carboxyl groups, the PGMA@Fe₃O₄@SiO₂-COOH microspheres acquire a saturation magnetization of up to 17.73 emu/g. These microspheres also exhibit a dense SiO₂ layer on the surface, a high concentration of carboxyl groups (0.829 mmol/g), excellent dispersion stability, and rapid magnetic responsiveness. Consequently, it demonstrates excellent efficacy in isolating DNA from Salmonella typhi, monkeypox virus, and clinical swab samples.

Supplementary Information The online version contains supplementary material available at <https://doi.org/10.1007/s10904-023-02975-4>.

Author Contributions TX: Conceptualization, Methodology, Formal analysis, Writing (original draft, review and editing). YW: Resources, Formal analysis, Methodology. PA: Project administration, Formal analysis, Supervision. SL, WD, DC: Resources, Methodology, Supervision. ML: Formal analysis, Methodology. XQ and XF: Conceptualization, Methodology, Project administration, Investigation, Supervision, Writing (review and editing).

Funding This research was financially supported from the “Leading Goose” R & D program (Grant No. 2022C01142) of Zhejiang Province, and the Collaboration Program (Grant No. 2022-KYY-509108-0023) of ZJU-Assure Research & Development Center.

Data Availability All data generated or analyzed during this study are included in the figures and tables in this published article and its Supplementary Information file.

Declarations

Conflict of interest There are no competing financial interests or personal relationships that could have appeared to influence the work to declare.

Ethical Approval Not Applicable.

References

1. Y.C. Guillaume, E. Peyrin, M. Thomassin, A. Ravel, C. Grosset, A. Villet, J.-F. Robert, C. Guinard, *Anal. Chem.* **72**, 4846–4852 (2000)
2. J. Carlstedt, D. Lundberg, R.S. Dias, B. Lindman, *Langmuir* **28**, 7976–7989 (2012)
3. X. Geng, C. Ke, G. Chen, P. Liu, F. Wang, H. Zhang, X. Sun, *J. Chromatogr. A* **1216**, 3553–3562 (2009)
4. J.A. Asenjo, B.A. Andrews, *J. Chromatogr. A* **1238**, 1–10 (2012)
5. Z. Liu, Y. Liu, S. Shen, D. Wu, *J. Mater. Chem. B* **6**, 366–380 (2018)
6. S. Liu, B. Yu, S. Wang, Y. Shen, H. Cong, *Adv. Colloid Interface Sci.* **281**, 102165 (2020)

7. Q. Yang, Y. Dong, Y. Qiu, X. Yang, H. Cao, Y. Wu, *Colloids Surf. B* **191**, 111014 (2020)
8. M. Ge, J. Zhang, Z. Gai, R. Fan, S. Hu, G. Liu, Y. Cao, X. Du, Y. Shen, *Chem. Eng. J.* **404**, 126427 (2021)
9. M. Zandieh, J. Liu, *Bioconjugate Chem.* **32**, 801–809 (2021)
10. Y. Gao, Y. Tang, L. Gao, Y. Niu, R. Gao, X. Chen, Y. Hao, S. Wang, *Anal. Chim. Acta* **1161**, 338475 (2021)
11. J. Wang, H. Guan, Q. Liang, M. Ding, *Compos. B* **198**, 108248 (2020)
12. X. Zheng, C. Shen, Y. Guo, H. Zheng, *RSC Adv.* **13**, 7413–7424 (2023)
13. Y. Chen, F. Zhang, X. Shi, M. Lu, K. Qin, Q. Feng, R. Guo, *J. Environ. Chem. Eng.* **10**, 108164 (2022)
14. M.J. Kishor Kumar, J.T. Kalathi, *Langmuir* **35**, 13923–13933 (2019)
15. J. Yao, F. Gao, X. Liang, Y. Li, Y. Mi, Q. Qi, J. Yao, Z. Cao, *Colloids Surf. A* **570**, 449–461 (2019)
16. D. Horák, H. Hlídková, Š. Trachtová, M. Šlouf, B. Rittich, A. Španová, *Eur. Polym. J.* **68**, 687–696 (2015)
17. J. Ugelstad, A. Berge, *Fresenius' J. Anal. Chem.* **330**, 328–328 (1988)
18. X. Cao, Q. Xie, S. Zhang, H. Xu, J. Su, J. Zhang, C. Deng, G. Song, *J. Chromatogr. A* **1607**, 460402 (2019)
19. Y. Yin, M. Chen, S. Zhou, L. Wu, *J. Mater. Chem.* **22**, 11245–11251 (2012)
20. X. She, J. Li, J. Zhu, T. Huang, Y. Li, *J. Chromatogr. A* **1637**, 461809 (2021)
21. H. Meng, Z. Zhang, F. Zhao, T. Qiu, J. Yang, *Appl. Surf. Sci.* **280**, 679–685 (2013)
22. S. Mavila, H.R. Culver, A.J. Anderson, T.R. Prieto, C.N. Bowman, *Angew. Chem. Int. Ed.* **61**, e202110741 (2022)
23. X. Sun, L. Yang, H. Xing, J. Zhao, X. Li, Y. Huang, H. Liu, *Chem. Eng. J.* **234**, 338–345 (2013)
24. L.-H. Xiao, T. Wang, T.-Y. Zhao, X. Zheng, L.-Y. Sun, P. Li, F.-Q. Liu, G. Gao, A. Dong, *Int. J. Mol. Sci.* **14**, 7391–7404 (2013)
25. B. Jia, M.J. Cui, C.C. Yang, S.Y. Hu, Y.K. Lv, *J. Appl. Polym. Sci.* **136**, 48019 (2019)
26. B. Yu, B. Yang, G. Li, H. Cong, *J. Mater. Sci.* **53**, 6471–6481 (2018)
27. X. Fan, J. Liu, X. Jia, Y. Liu, H. Zhang, S. Wang, B. Zhang, H. Zhang, Q. Zhang, *Nano Res.* **10**, 2905–2922 (2017)
28. D. Yuan, L. Chen, L. Yuan, S. Liao, M. Yang, Q. Zhang, *Chem. Eng. J.* **287**, 241–251 (2016)
29. W. Li, Q. Liu, R. Chen, J. Yu, H. Zhang, J. Liu, R. Li, M. Zhang, P. Liu, J. Wang, *Inorg. Chem. Front.* **5**, 1321–1328 (2018)
30. Z. Zhang, P. He, W. Ma, P. Zuo, X. Liu, Q. Zhuang, *Adv. Funct. Mater.* **33**, 2302212 (2023)
31. B. Liu, Z. Fu, Y. Han, M. Zhang, H. Zhang, *Colloid Polym. Sci.* **295**, 749–757 (2017)
32. T. Yamamoto, M. Nakayama, Y. Kanda, K. Higashitani, *J. Colloid Interface Sci.* **297**, 112–121 (2006)
33. T. Yamamoto, *J. Colloid Interface Sci.* **290**, 1023–1031 (2012)
34. R.M. Cornell, P.W. Schindler, *Colloid Polym. Sci.* **258**, 1171–1175 (1980)
35. B.K. Sodipo, O.A. Noqta, A.A. Aziz, M. Katsikini, F. Pinakidou, E.C. Paloura, *J. Alloys Compd.* **938**, 168558 (2023)
36. K.Y. Yoon, Z. Xue, Y. Fei, J.H. Lee, V. Cheng, H.G. Bagaria, C. Huh, S.L. Bryant, S.D. Kong, V.W. Ngo, A.-R. Rahmani, M. Ahmadian, C.J. Ellison, K.P. Johnston, *J. Colloid Interface Sci.* **462**, 359–367 (2016)
37. A. Atrei, F.F. Mahdizadeh, M.C. Baratto, A. Scala, *Appl. Sci.* **11**, 6974 (2021)
38. L.L. Félix, M.A. Rodríguez Martínez, D.G. Pacheco Salazar, J.A. Huamani Coaquira, *RSC Adv.* **10**, 41807–41815 (2020)
39. H.Y. Hah, S. Gray, C.E. Johnson, J.A. Johnson, V. Kolesnichenko, P. Kucheryavy, G. Goloverda, *J. Magn. Magn. Mater.* **539**, 168382 (2021)
40. A. Spivakov, C.-R. Lin, Y.-C. Chang, C.-C. Wang, D. Sarychev, *Nanomaterials* **10**, 1888 (2020)
41. S. Upadhyay, K. Parekh, B. Pandey, *J. Alloys Compd.* **678**, 478–485 (2016)
42. A. Tahir, A. Saeed, I. Ramzan, S.S. Hayat, W. Ahmad, S. Naeem, M. Afzal, A. Mukhtar, T. Mehmood, B.S. Khan, *Appl. Nanosci.* **11**, 1857–1865 (2021)
43. H. Macková, F. Oukacine, Z. Plichta, M. Hrubý, J. Kučka, M. Taverna, D. Horák, *J. Colloid Interface Sci.* **421**, 146–153 (2014)
44. X. Zhao, Z. Wei, Z. Zhao, Y. Miao, Y. Qiu, W. Yang, X. Jia, Z. Liu, H. Hou, *A.C.S. Appl. Mater. Interfaces* **10**, 6608–6617 (2018)
45. F. Qu, J. Liu, Y. Wang, S. Wen, Y. Chen, X. Li, S. Ruan, *Sens. Actuators B* **199**, 346–353 (2014)
46. X. Li, K. Cui, Z. Guo, T. Yang, Y. Cao, Y. Xiang, H. Chen, M. Xi, *Chem. Eng. J.* **379**, 122324 (2020)
47. X. Lv, W. Huang, X. Ding, J. He, Q. Huang, J. Tan, H. Cheng, J. Feng, L. Li, *J. Rare Earths* **38**, 1288–1296 (2020)
48. X. Liang, J. Fan, Y. Zhao, R. Jin et al., *J. Rare Earths* **39**, 579–586 (2021)
49. C. Wang, J. Zhuang, S. Jiang, J. Li, W. Yang, *J. Nanopart. Res.* **14**, 1202 (2012)
50. K. Murugesan, C.A. Hogan, Z. Palmer, B. Reeve, G. Theron, A. Andama, A. Somoskovi, A. Steadman, D. Madan, J. Andrews, J. Croda, M.K. Sahoo, A. Cattamanchi, B.A. Pinsky, N. Banaei, *J. Clin. Microbiol.* **57**, e00782–e819 (2019)
51. W. Tang, R. Mi, L. Wang, H. Chen, *Sens. Actuators B* **340**, 129699 (2021)
52. G. Liu, Q. Zhang, K. Wang, J. Niu, A. Gao, M. Chen, Z. Yang, C. Zhou, G. Gao, D. Cui, *A.C.S. Appl. Nano Mater.* **6**, 3344–3356 (2023)
53. H. Cui, W. Song, X. Ru, W. Fu, L. Ji, W. Zhou, Z. Zhao, G. Qu, X.-F. Yu, G. Jiang, *Talanta* **258**, 124479 (2023)

Publisher's Note Springer Nature remains neutral with regard to jurisdictional claims in published maps and institutional affiliations.

Springer Nature or its licensor (e.g. a society or other partner) holds exclusive rights to this article under a publishing agreement with the author(s) or other rightsholder(s); author self-archiving of the accepted manuscript version of this article is solely governed by the terms of such publishing agreement and applicable law.